Catalysis Today 432 (2024) 114603

Contents lists available at ScienceDirect

Catalysis Today

journal homepage: www.elsevier.com/locate/cattod

In-situ FT-IR study of alcohols degradation in the gas phase using different TiO_2 composites

Andrea Illana [a,b,*], José Miguel Doña-Rodríguez [a], Alison Robles [a], Óscar M. González-Díaz [a], Elisenda Pulido-Melián [a], Luis Miguel Azofra [a], Javier Araña [a,**]

[a] Instituto de Estudios Ambientales y Recursos Naturales (i-UNAT), Universidad de Las Palmas de Gran Canaria (ULPGC), Campus de Tafira, Las Palmas de Gran Canaria 35017, Spain

[b] Universidad Complutense de Madrid, Avda. Complutense s/n, Madrid 28040, Spain

ARTICLE INFO

Keywords:
TiO_2
FT-IR
Composites
Aggregates
Gas-phase

ABSTRACT

Herein, we present an *in-situ* FT-IR study analysing the interactions and photocatalytic degradation of *1*-butanol and methanol in the gas phase through the catalysts Hombikat-b (commercial) and EST-1023 (synthesised in lab), as well as composites of them in a range of pH between 5 and 9. Composite Homb@EST at neutral pH (Homb@EST-pH7) has presented a photocatalytic efficiency much higher than that of the separate catalysts in both the degradation of alcohols and carboxylates. Characterisation analyses have shown that EST-1023 exhibits low surface area and surface hydroxylation, which suggests practically no adsorption of alcohols at the initial stages of the process. Notwithstanding, we have determined a large concentration of surface electronic traps in EST-1023. On the contrary, Hombikat-b presents high surface area and surface hydroxylation, leading to high adsorption rates of the studied alcohols. Aggregate distribution, SEM, and HR-TEM studies have shown that neutral pH is the most appropriate condition to aggregate both catalysts, generating the so-called composite Homb@EST-pH7. The high photocatalytic capability of this composite is attributed to the transfer of photo-generated electrons from the Hombikat-b nanoparticles to the electron traps present in EST-1023, which implies a decrease in the recombination speed of the photogenerated electron-hole (e^-/h^+) pairs.

1. Introduction

Photocatalysis has emerged as a promising technique for the removal of pollutants present in air and aqueous effluents, however the development of novel, more efficient photocatalysts remains as a challenge [1,2]. Titanium dioxide (TiO_2), ubiquitous semiconductor in the photocatalytic literature, is amongst the most used photocatalytic materials, notwithstanding, the high rate for the recombination of excited electrons and photogenerated holes (e^-/h^+) is a drawback whose resolution centres an important part of the efforts in current photocatalytic research [3,4]. Literature reports that TiO_2 Evonik (formerly Degussa) P25 commercial catalyst exhibits, in general, superior photocatalytic efficiency, which has allowed it to serve as a reference in many investigations [5–7]. Based on EPR analysis carried out by Thurnauer and co-workers, P25 presents a morphology of nanoclusters with a core constituted by rutile phase surrounded by anatase, being the interface between both causative of favour the rapid transfer of electrons and turning rutile into a sink of photogenerated electrons [8]. Besides, P25 exhibits a low surface area ($\sim 50\ m^2\ g^{-1}$) [9,10].

In reference to the synthesis of novel materials favouring an efficient separation of photo-generated electrons and holes, Liu *et al.* [11] reported the loading of TiO_2 with ultra-small Cu_2O nanoparticles. Based on data provided by authors, an atomic ratio of Ti:Cu 30:1 for the heterojunction Cu_2O/TiO_2 shows the best activity due to its balance in light harvest and electron transfer rate in the degradation of phenol under visible light. More recently, He *et al.* [12] communicated a facile sol-gel route for the formation of anatase/rutile nanocomposites, attributing the best results for the photodegradation of dye methylene blue under UV illumination to an optimal ratio of 69:31 rutile:anatase at pH 1, together with a smaller average particle size, and the presence of a specific crystalline phase exposed to the reactive medium. In this line, the heterojunction of the host semiconductor with other low band-gap

* Corresponding author at: Instituto de Estudios Ambientales y Recursos Naturales (i-UNAT), Universidad de Las Palmas de Gran Canaria (ULPGC), Campus de Tafira, Las Palmas de Gran Canaria 35017, Spain

** Corresponding author.

E-mail addresses: andrea.illana@ext.ulpgc.es (A. Illana), javier.arana@ulpgc.es (J. Araña).

https://doi.org/10.1016/j.cattod.2024.114603

Received 7 November 2023; Received in revised form 26 January 2024; Accepted 19 February 2024

Available online 20 February 2024

metal oxides having different band edge positions has been successfully addressed in a recent study published by Konwar and co-workers [13]. In order to improve and optimise the photocatalytic efficiency, different synthetic strategies for TiO_2 have been followed, as well as surface modifications with noble metal nanoparticles, combination with adsorbents, or preparation of composites with different semiconductors [14–16]. Sol-gel and hydrothermal methods are amongst the synthetic strategies used to obtain nanostructured photocatalysts only constituted by anatase phase [17–19], even presenting larger surfaces areas than in P25 commercial catalyst ($\sim$90 $m^2\ g^{-1}$) [20]. Thus, nano-structuring of TiO_2 reduces the distance between the photogeneration centres of e^-/h^+ pairs and the surface where the formation of radicals and their reaction with contaminants takes place. However, these catalysts formed by nanoparticles also generate a greater number of pairwise recombination centres on the surface [21]. Besides, the synthesis of TiO_2/activated carbon composites has also given promising results [22,23].

The recombination rate of the photogenerated charges can also be modified by the presence of structural defects on the surface and in the crystalline lattice of the semiconductors [24,25]. These defects, such as oxygen vacancies (O_{vac}), modify the distribution of bonding and antibonding orbitals in the conduction (CB) and valence bands (VB), rising to new states that modify the band gap and act as electron traps [26,27], *i.e.*, the new intra-bands can influence the behaviour of the charge carriers since they offer new centres available for the relaxation of photogenerated electrons between CB and VB.

Against this background, in the present work two catalysts based on TiO_2 have been selected to form composites that can improve their efficiency with respect to that of the separate materials. On the one hand, the commercial catalyst Hombikat-b presents a very large surface area ($\sim$330 $m^2\ g^{-1}$) [28,29], although a very low photocatalytic activity in several studies carried out in aqueous solution [30–32]. On the other, the catalyst EST-1023 synthesised in lab exhibits a much higher photocatalytic activity than other commercial ones in different studies, although characterised by very low surface areas ($\sim$15 $m^2\ g^{-1}$) [33,34]. Its combination at different pH conditions results in the formation of composites that show enhanced properties with respect the constituted catalysts separately.

2. Experimental

2.1. Catalysts

Two catalysts were used, the commercial Hombikat-b (Hombikat UV 100 from Sachtleben Chemie GmbH) and the laboratory-synthesised EST-1023. The latter was synthesised using the following process: a mixture of 40 mL of ethanol and 17 mL of titanium (IV) butoxide (TBT) were added dropwise to a solution of 40 mL of ethanol, 15 mL of water and 463 μL of sulphuric acid (96% PANREAC). After this process, the mixture was maintained 30 minutes under stirring (1500 rpm). The gel obtained was dried at 373 K for 24 h, and subsequently sieved with a 63 μm sieve. Finally, the photocatalyst was subjected to an annealing treatment at 973 K for 3.5 h (heating rate of 277 K min^{-1}).

2.2. Analysis techniques

Phase composition of catalysts were estimated from X-ray diffraction (XRD) patterns recorded on a Bruker model D8 Advance diffractometer equipped with a Ni filter and LINXEYE detector using Cu Kα radiation (λ = 1.5418 Å). The N_2 adsorption-desorption isotherms at 77 K were performed with 3 P INSTRUMENTS, model Micro 300. The samples were outgassed under vacuum at 150 ºC for 12 h. The specific surface area was determined by the Brunauer–Emmett–Teller (BET) method, the total volume at relative pressure of 0.99, and the mesopore volume with the BJH method with the Harkins–Jura t-curve. Particle size distribution (PSD), which gives an idea of the distribution of the particle aggregates, was measured by a laser diffraction method. For this purpose, a Mastersizer 3000 equipped with a Hydro SM wet sample dispersion unit was used. Superficial morphology and the interactions between aggregates were observed by a Hitachi TM3030 scanning electron microscope (SEM), operating at an accelerated voltage of 15 kV and 9 μm of working distance, as well as by a JEOL JEM 2100 high-resolution transmission electron microscope (HR-TEM), at an accelerating voltage of 200 kV. HR-TEM specimens were prepared by drop-casting technique, from a suspension of the powder catalyst dispersed in isopropanol by sonication. UV-Vis diffuse reflectance spectra (DRS) were obtained using a Varian Cary 5 spectrophotometer, and the reflection data were converted to absorbance through the standard Kubelka–Munk method [35,36]. A Thermo Scientific-Nicolet iS10 spectrophotometer was used for the Fourier transform infrared (FT-IR) studies. The catalyst was placed between two CaF_2 mirrors, and a 4000–1000 cm^{-1} measurement range, 2 cm^{-1} resolution, and forward/backward mirror speeds of 10 kHz/6.2 kHz, respectively, were used.

2.3. Synthesis of composites

The selected catalysts were mixed in a 1:1 mass ratio in 20 mL of deionised water, by magnetic stirring at 200 rpm. Stirring was maintained for 2 h before proceeding to the adjustment of the different pH (5, 7, 9), with the addition of NaOH or HCl aqueous solutions 0.1 M. After 24 h under stirring, the pH value was checked again and, subsequently, the samples were dried in an oven at 423 K for 24 h.

2.4. Photocatalytic tests

1-butanol (*1*-BuOH) and methanol (MeOH) photodegradation studies were carried out in a FT-IR spectrophotometer at 298.15 K. The catalyst was previously impregnated with alcohol/air vapour dosed at room temperature for 120 min. The impregnation system consisted of a vessel containing the water/alcohol solution and air bubbled at a flow rate of 50 $cm^3\ min^{-1}$. The resulting gas containing water/alcohol vapours was introduced in a 15 cm long, 4 mm diameter cylindrical glass reactor containing 0.02 g of the catalyst. After this, the catalysts were carefully taken from the reactor under air atmosphere and placed in the cell with CaF_2 windows for FT-IR analyses. Water reference spectrum was subtracted from each spectrum. Once the first spectrum was obtained, the cell was irradiated during different periods of time and analysed by FT-IR again. A 60 W Philips Solarium HB175 equipped with four 15 W Philips CLEO fluorescent tubes with emission between 300 and 400 nm (λ_{max} = 365 nm, 9 mW) was used as UV source in the degradation studies. In this way, the adsorption of the selected molecules onto the catalyst surface and their reaction under irradiation were studied. Desorption studies of the adsorbed alcohols have been carried out exposing the cell with the catalyst to irradiation but covered. In these tests, no changes have been observed with respect the initial spectrum. The carboxylates and carbonates identified have been checked with the corresponding standards. On the other hand, the identified intermediates coincide with those described in the literature for the degradation of *1*-butanol and methanol in the gas phase [16,37].

2.5. DFT studies

Reaction free energies for Eqs. (1) to (24) for the different states along the degradation of *1*-BuOH and MeOH have been estimated through density functional theory (DFT) calculations using the B3LYP functional [38,39] and the split-valence double-ζ SVP basis set [40] in vacuum. Harmonic frequency calculations were performed to confirm the nature of the stationary points, *i.e.*, minima or first-order transition states (TS) with none and one imaginary frequency, respectively. All calculations were carried out through the facilities provided by the NWChem package (version 6.8.1) [41,42].

3. Results and discussions

3.1. Characterisation of materials

The commercial catalyst Hombikat-b is only composed by the anatase phase with a particle size of 8 nm. On the other hand, the EST-1023 catalyst is composed of 70% of the anatase phase and 30% of the rutile phase, with a particle size between 62.3 and 96.1 nm, respectively (see Appendix A. Supplementary data). As indicated in the experimental section, the composites were synthesised by making 1:1 mixture of these two catalysts at different pH conditions. Table 1 indicates the surface area, isoelectric point, total pore volume, and mesopore volume for the individual catalysts as well as for the composites synthesised in this work. According to the t-plot method, the samples show no microporosity. The small difference between total volume and mesoporosity is due to macroporosity, as the measuring range of the 3 P INSTRUMENTS instrument is up to 500 nm in diameter. The individual catalysts were also exposed to different pH conditions with the objective of determining modifications in these properties, but no significant changes were identified.

3.1.1. Aggregate distribution analysis

Being the objective of this work the synthesis of composites Homb@EST, the existence of interactions between particles of different size of the constituting materials may improve the photocatalytic activity of the composite. One way to determine changes in the interactions due to the presence of particles of different size, it is through the analysis of aggregates or agglomerates generated as result of the mixing process. The formation of aggregates is due to the destabilisation of the nanoparticles and mainly depends on the size, shape, and surface modifications [43], modulating these the presence of electrostatic repulsions and van der Waals interactions. When electrostatic repulsions are eliminated by neutralisation of surface charges, the attractive van der Waals interactions are dominant and the size of the aggregate increases. In general, in large nanoparticles the repulsive interactions are greater due to the high charge on their surface and, on the contrary, in smaller nanoparticles the repulsive interactions are lower due to the small surface charge [44].

Fig. 1**a** shows the size of aggregates generated in the separate catalysts, Hombikat-b and EST-1023. As previously indicated, the Homb@EST composites have been synthesised by varying the pH to 5, 7, and 9. Fig. 1**b** shows the distribution of the composite synthesised at pH 7 (Homb@EST-pH7) and of the separate materials at the same pH. In Hombikat-b, a bimodal bell-shaped Gaussian distribution is observed with central values at 1.5 and 62.8 μm, respectively (see Fig. 1**a**), although the proportion of the second being greater than the first [45]. When pH is modified to 7 (pH at the conditions of synthesis has been measured in 3.74 at 26.9 ºC, regulating this with NaOH aqueous solution 0.1 M), the proportion of the smallest aggregates decreases from 4% to 2.5% and those with central value at 62.7 μm disaggregate into smaller aggregates (55.3 μm). (See Fig. 1**b**). Catalyst EST-1023 presents a single type of aggregates with a central value in its bell-shaped Gaussian distribution at 42.8 μm (see Fig. 1**a**). However, when treated at pH 7 it decomposes into smaller aggregates with central values at 2.7 and 9.2 μm, while other portion results in agglomeration with central value at 62.7 μm. On the other hand, Gaussian distribution in Homb@EST-pH7 composite indicates that the larger aggregates of EST-pH7 and Homb-pH7, whose central values were at 9.2, 55.3, and 62.7 μm, are redistributed, as it probes a wider and more centred Gaussian distribution with central value at 29.6 μm. That is, there has been an interaction between the larger aggregates of Homb-pH7 and EST-pH7.

The same protocol was followed to analyse the distribution of aggregates at pH 5 and 9. In these cases, they coincide with the sum of those obtained from the separate material at the studied pH conditions. That is, the interaction between the aggregates/particles of Hombikat-b and EST-1023 takes place in aqueous suspension at neutral pH. The isoelectric point of EST-1023 is 6.6 while for Hombikat-b it is 6.1. At higher pH values or for particles of lower size, these will be electrically charged, and the repulsive forces will be greater than the van der Waals forces that favour the interactions.

3.1.2. SEM, HR-TEM, and UV-Vis analysis

In order to confirm the observed interactions between the Hombikat-b and EST-1023 aggregates, scanning electron microscopy (SEM) and high resolution-transmission electron microscopy (HR-TEM) analyses were carried out. Fig. 2**a** corroborates the results observed in Fig. 1**a**, since spherical aggregates of 1.5 and 55.3–62.8 μm can be observed for Homb-pH7. As seen at Fig. 2**a**, the presence of amorphous aggregates similar size to those observed in Fig. 1**b** for EST-pH7 is also seen. On the other hand, in the SEM micrographs and HR-TEM image of the Homb@EST-pH7 composite (see Fig. 2**c** and Fig. 2**d**), spherical aggregates of Hombikat-b are observed covering the aggregates of EST-1023, thus confirming the interactions already described in the aggregation studies.

Fig. 3 shows the UV-Vis DRS spectra of the Hombikat-b, EST-1023 and Homb@EST-pH7, in the form of a normalized Kubelka–Munk function: $F(R_\infty) = \frac{\alpha}{S} = \frac{(1-R_\infty)^2}{2R_\infty}$; α is the absorption coefficient, S is the scattering coefficient of the powder, and R_∞ is the diffuse reflectance in an infinitely thick layer. In Homb@EST-pH7 an absorption shift towards red is observed. This can be attributed to the creation of mid-gap states in the bandgap of the titanium atoms of the Hombikat-b as consequence of the interaction with EST-1023. This interaction presents high concentrations of oxygen vacancies, as can be observed in the UV-Vis absorption spectra. Similar behaviours have been observed in other heterojunctions described in the literature [13,46,47].

These results would indicate that at pH 7 the partial disintegration of the Hombikat-b and EST-1023 moieties would take place, as well as the interaction between them (see Scheme 1).

3.1.3. FT-IR analysis

The FT-IR spectra for Homb-pH7, EST-pH7, and Homb@EST-pH7 catalysts are shown in Fig. 4. In all the spectra it can be observed bands at 3400, 3200, and 1640 cm^{-1} attributed to stretching and bending modes of adsorbed water, respectively [48–51]. As can be seen, the surface hydration is greater in Homb-pH7 and Homb@EST-pH7 catalysts. Another aspect to highlight in these spectra is the position of the baseline since an increase of this has been correlated with the presence of shallow electron traps [52–55], in our case represented by oxygen vacancies. From these spectra, it is indicated that EST-pH7 is the catalyst that presents the greatest number of sub- or surface oxygen vacancies. In Homb@EST-pH7, the baseline is higher than in Homb-pH7 but significantly lower than in EST-pH7.

Table 1
Surface area, isoelectric point, total pore volume, and mesopore volume for catalysts used in this work.

Catalyst	Surface area ($m^2\ g^{-1}$)	Isoelectric point	$V_{total\ pore}$ ($cm^3\ g^{-1}$)	$V_{mesopore}$ ($cm^3\ g^{-1}$)
EST-1023	28.2	6.6	0.088	0.066
Hombikat-b	242.5	6.1	0.39	0.34
Homb@EST-pH5	119.8	6.4	0.22	0.18
Homb@EST-pH7	117.7	6.3	0.23	0.18
Homb@EST-pH9	115.0	8.3	0.24	0.18

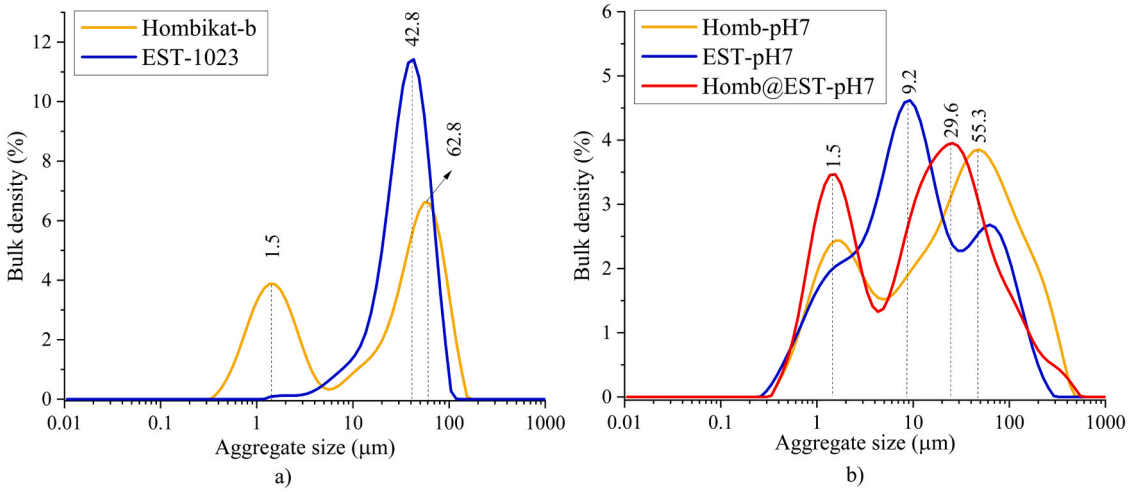

Fig. 1. Size of aggregates in: a) Hombikat-b and EST-1023; and b) Homb-pH7, EST-pH7, and Homb@EST-pH7.

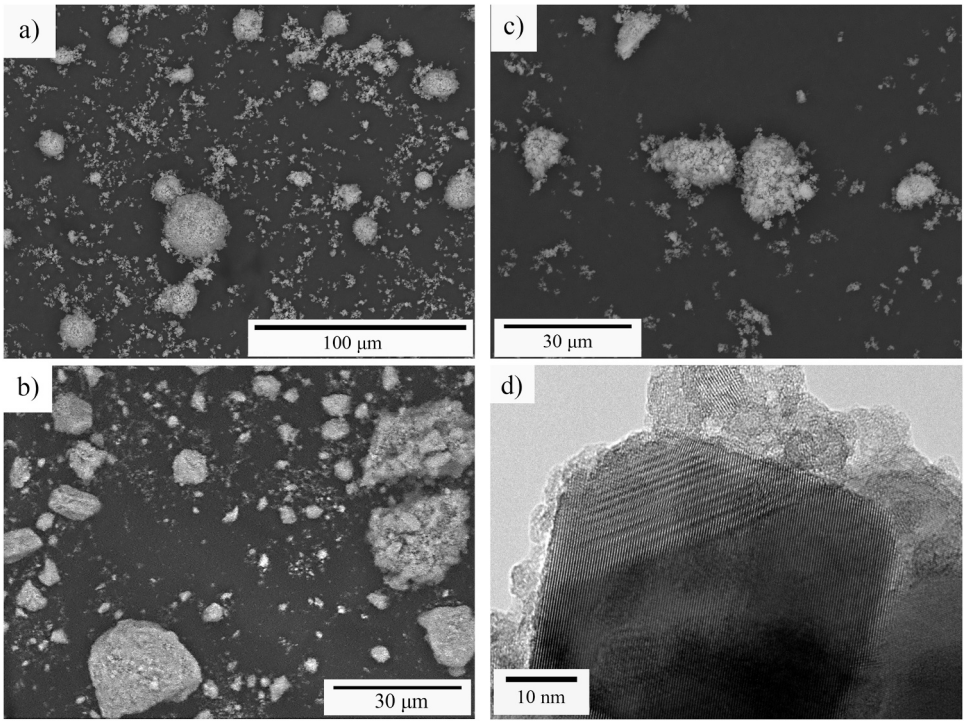

Fig. 2. SEM micrographs of: a) Homb-pH7; b) EST-pH7; c) Homb@EST-pH7; and d) HR-TEM image of Homb@EST-pH7.

3.2. Photocatalytic degradation of 1-butanol and methanol in the gas phase

To compare the photocatalytic efficiency of the new composite against the constituted photocatalysts separately for the degradation of alcohols in the gas phase, *1*-BuOH, and MeOH, have been used as probe molecules to analyse their interactions and evolution under UV-Vis illumination using FT-IR.

3.2.1. Photocatalytic degradation of 1-butanol

Fig. 5 displays the spectra for the interaction of *1*-BuOH and its evolution under illumination with the Hombikat-b and Homb@EST-pH7 photocatalysts at different reaction times. Initially, bands at 1466 and 1382 cm^{-1} are attributed to the asymmetric and symmetric deformation vibrations of the CH_3 group, respectively, and bands at 1075, 1045, and 1029 cm^{-1} are attributed to the tension vibrations of the C—O group [56,57]. Interestingly, throughout the first minutes under illumination, a progressive decrease of the band at 1075 cm^{-1} is observed appearing new bands at 1715, 1570, 1532, and 1440 cm^{-1}. Thus, bands at 1570, 1532, and 1440 cm^{-1} are attributed to the antisymmetric ν_{as}(COO) and symmetric ν_s(COO) vibrations of adsorbed carboxylates on the catalytic surface, such as butanoates, acetates, or formates [58,59].

Fig. 6 shows the evolution of the bands at 1075 and 1570 cm^{-1}, attributed, as mentioned above, to the tension vibration of the C—O group of *1*-BuOH and the ν_{as}(COO) vibration of the generated carboxylates during the illumination with the Hombikat-b, Homb-pH7, and Homb@EST-pH7 catalysts, respectively. At time 0 min, the spectra indicate a similar behaviour for the adsorption of *1*-BuOH in both Homb-pH7 and in Homb@EST-pH7. Despite the pattern of each spectrum is similar, in the second we observe a lower intensity. This may be due to the different distribution of aggregates observed in the characterisation studies. The photocatalytic degradation of *1*-BuOH is significantly

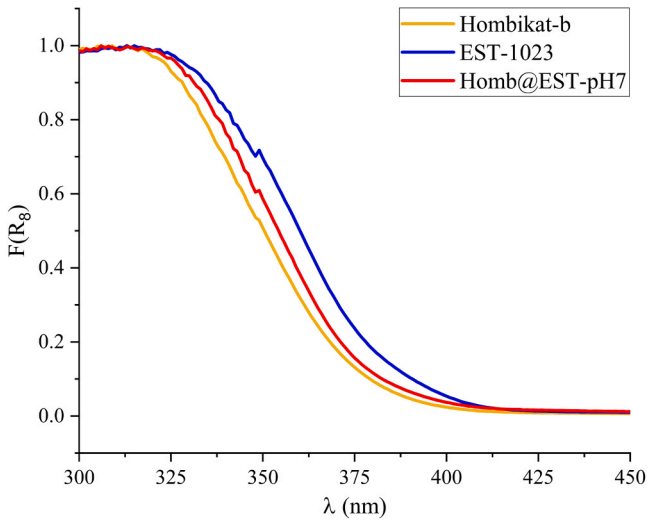

Fig. 3. UV-Vis DRS spectra of Hombikat-b, EST-1023, and Homb@EST-pH7.

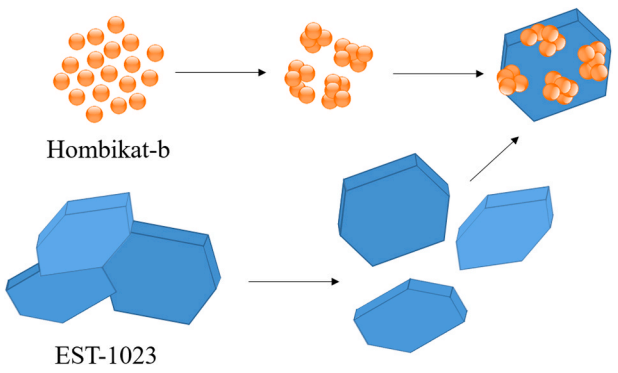

Scheme 1. Schematic procedure for the interaction between Hombikat-b and EST-1023 to form the composite.

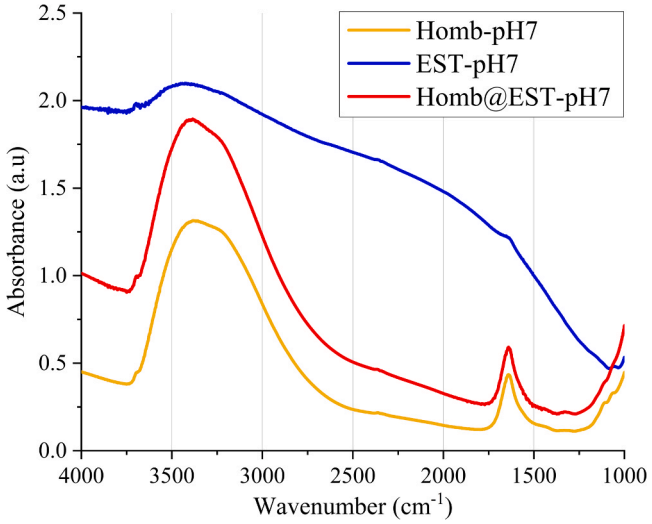

Fig. 4. FT-IR spectra of Homb-pH7, EST-pH7, and Homb@EST-pH7.

slower in Hombikat-b and Homb-pH7 compared to that of the composite. However, the generated carboxylates in Homb-pH7 are not degraded, while those formed in Hombikat-b are degraded although very slowly. On the other hand, in the Homb@EST-pH7 composite the formation and rapid degradation of these carboxylates is clearly observed. In the final spectra of Homb@EST-pH7, bands at 1715, 1690, 1630, 1415 cm^{-1} are seen, which are attributed to adsorbed carbonates generated from the photocatalytic degradation process. FT-IR studies have also been carried out for *1*-BuOH under illumination with EST-1023 and EST-pH7 but the interaction of this alcohol with these catalysts is very low, specifically at trace level.

3.2.2. Photocatalytic degradation of methanol

Fig. 7 displays the spectra for the interaction of MeOH and its evolution under illumination with the Hombikat-b photocatalyst at different reaction times. Initially, bands at 1447 and 1040 cm^{-1} are observed, being attributed to $\delta_{as}(CH_3)$, $\delta_s(CH_3)$, $\delta(OH)$ in the plane of the adsorbed MeOH [60]. Under illumination, new bands appear at 1585, 1382, and 1358 cm^{-1} attributed to vibrations of ionic formates [61].

Fig. 8 shows the evolution under illumination of the bands at 1040 cm^{-1} of MeOH and the one at 1585 cm^{-1} attributed to the ionic formate with the Hombikat-b, Homb-pH7, and Homb@EST-pH7 photocatalysts. As observed in the studies with *1*-BuOH, the initial adsorption of MeOH is practically similar in Homb-pH7 and Homb@EST-pH7, while in Hombikat-b it is much lower. The degradation of MeOH is significantly faster with Homb@EST-pH7, so that after 60 min of reaction this is almost completely degraded, while with Homb-pH7 it takes 90 min. Likewise, the degradation of the generated formates is significantly faster when the composite acts as photocatalyst. In Hombikat-b and Homb-pH7, we appreciate that once the MeOH concentration has decreased significantly, then formates begin to degrade. On the contrary, for the composite both MeOH and formate degrade simultaneously, being the reason why the concentration determined on the surface is appreciably lower. These studies have been also carried out with EST and EST-pH7, but as was observed with *1*-BuOH, the initial adsorption of the alcohol is very low.

3.3. Discussion of results

The photocatalytic process starts with the formation of the e^-/h^+ pair in the semiconductor under illumination (Eq. 1). The formation of the $HO^\bullet$ radical takes place through the reaction of water with the holes (Eq. 2), leading to a series of chain reactions (Eqs. 3–8) which begin with the reaction of O_2 and the photogenerated electrons (Eq. 3). The degradation of the alcohol then starts with the abstraction of a hydrogen from the CH_2 moiety directly bounded with the alcoholic group. This takes place through the attack of the $HO^\bullet$ radical and forms the radical R-$CHOH^\bullet$ (Eq. 9) [62]. The aforementioned radical can react again with an $HO^\bullet$ radical resulting in the formation of the aldehyde and water (Eq. 10). Subsequently, the aldehyde is newly attacked by an $HO^\bullet$ radical, forming the radical R-$CHOHO^\bullet$ (Eq. 11) which, when reacting with O_2 or another $HO^\bullet$ radical, would form the corresponding carboxylic acid (Eq. 12). In a next step, the carboxylic acid would react with h^+ or an $HO^\bullet$ radical (Eqs. 13–14) to form the carboxylate radical R-$COO^\bullet$. Finally, this decomposes forming CO_2 and the radical $R^\bullet$ (Eq. 15), the latter reacting with O_2 to form the respective aldehyde of shorter carbon chain (Eqs. 16–18). For the specific case of *1*-BuOH:

$$TiO_2 + h\nu \rightarrow h^+ + e^- \quad (1)$$

$$H_2O + h^+ \rightarrow HO^\bullet + H^+ \quad (2)$$

$$O_2 + e^- \rightarrow O_2^{\bullet-} \quad (3)$$

$$O_2^{\bullet-} + H^+ \rightarrow HO_2^\bullet \quad (4)$$

$$HO_2^\bullet + e^- \rightarrow HO_2^- \quad (5)$$

$$HO_2^- + H^+ \rightarrow H_2O_2 \quad (6)$$

$$HO_2^\bullet + HO_2^\bullet \rightarrow H_2O_2 + O_2 \quad (7)$$

$$H_2O_2 + e^- \rightarrow HO^\bullet + OH^- \quad (8)$$

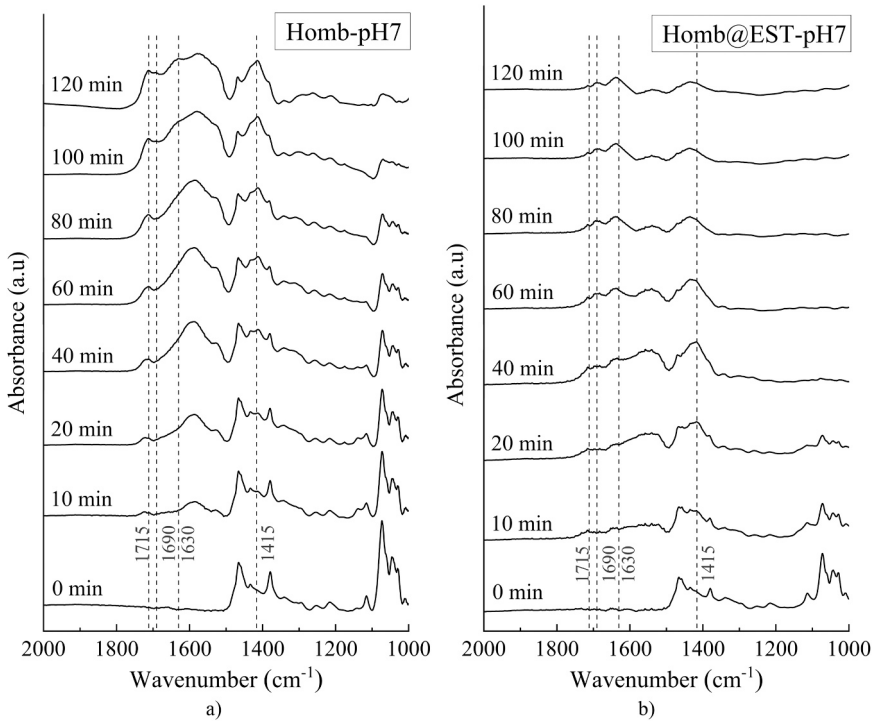

Fig. 5. FT-IR spectra along time for the photocatalytic degradation of *1*-BuOH in: a) Homb-pH7; and b) Homb@EST-pH7.

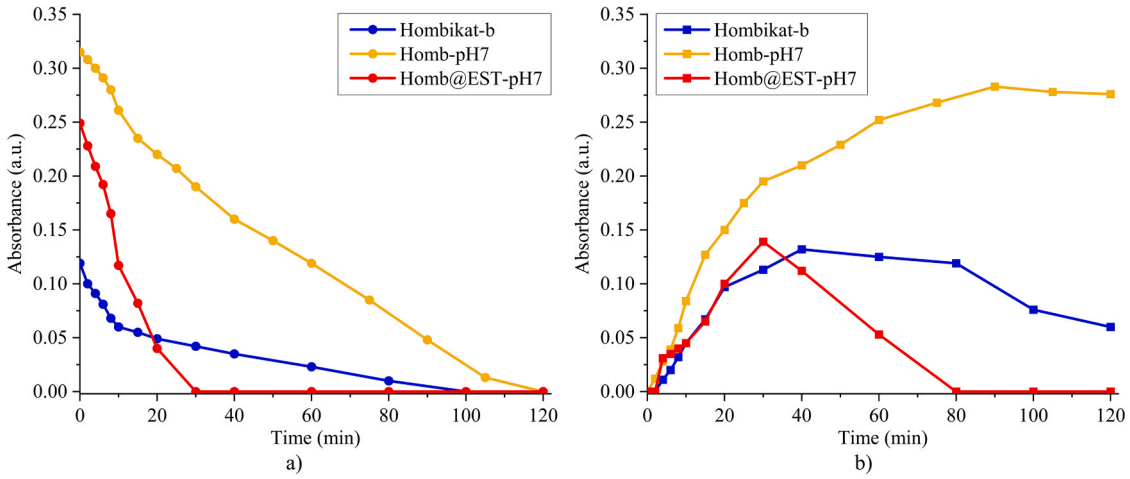

Fig. 6. Evolution of a) adsorbed *1*-BuOH (●) and b) generated carboxylates (■) for Hombikat-b, Homb-pH7 and Homb@EST-pH7.

$CH_3CH_2CH_2CH_2OH + HO^{\bullet} \rightarrow CH_3CH_2CHOH^{\bullet} + H_2O$, $\Delta G = -46.4$ *kcal/mol* (9)

$CH_3CH_2CH_2CHOH^{\bullet} + HO^{\bullet} \rightarrow CH_3CH_2CH_2CHO + H_2O$, $\Delta G = -109.8$ *kcal/mol* (10)

$CH_3CH_2CH_2CHO + HO^{\bullet} \rightarrow CH_3CH_2CH_2CHOHO^{\bullet}$, $\Delta G = -38.9$ *kcal/mol* (11)

$CH_3CH_2CH_2CHOHO^{\bullet} + HO^{\bullet} \rightarrow CH_3CH_2CH_2COOH + H_2O$, $\Delta G = -133.2$ *kcal/mol* (12)

$CH_3CH_2CH_2COOH + HO^{\bullet} \rightarrow CH_3CH_2CH_2COO^{\bullet} + H_2O$, $\Delta G = -34.2$ *kcal/mol* (13)

$CH_3CH_2CH_2COO^{-} + h^{+} \rightarrow CH_3CH_2CH_2COO^{\bullet}$ (14)

$CH_3CH_2CH_2COO^{\bullet} \rightarrow CO_2 + CH_3CH_2CH_2^{\bullet}$, $\Delta G = -22.7$ *kcal/mol* (15)

$CH_3CH_2CH_2^{\bullet} + O_2 \rightarrow CH_3CH_2CH_2OO^{\bullet}$, $\Delta G = -19.8$ *kcal/mol* (16)

$2\ CH_3CH_2CH_2OO^{\bullet} \rightarrow 2\ CH_3CH_2CH_2O^{\bullet} + O_2$, $\Delta G = -12.0$ *kcal/mol* (17)

$CH_3CH_2CH_2O^{\bullet} + O_2 \rightarrow CH_3CH_2CHO + HO_2^{\bullet}$, $\Delta G = -26.6$ *kcal/mol* (18)

And for the case of MeOH (reaction free energies are shown only for the case of $HO^{\bullet}$ attack):

$CH_3OH + HO^{\bullet} \rightarrow CH_2OH^{\bullet} + H_2O$, $\Delta G = -44.2$ *kcal/mol* (19)

$CH_2OH^{\bullet} + HO^{\bullet}/O_2 \rightarrow CH_2O + H_2O/HO_2^{\bullet}$, $\Delta G = -106.1$ *kcal/mol* (20)

$CH_2O + HO^{\bullet} \rightarrow CH_2OOH^{\bullet}$, $\Delta G = -40.3$ *kcal/mol* (21)

$CH_2OOH^{\bullet} + HO^{\bullet} \rightarrow HCOOH + H_2O$, $\Delta G = -129.1$ *kcal/mol* (22)

$HCOOH + HO^{\bullet} \rightarrow HCOO^{\bullet} + H_2O$, $\Delta G = -34.4$ *kcal/mol* (23)

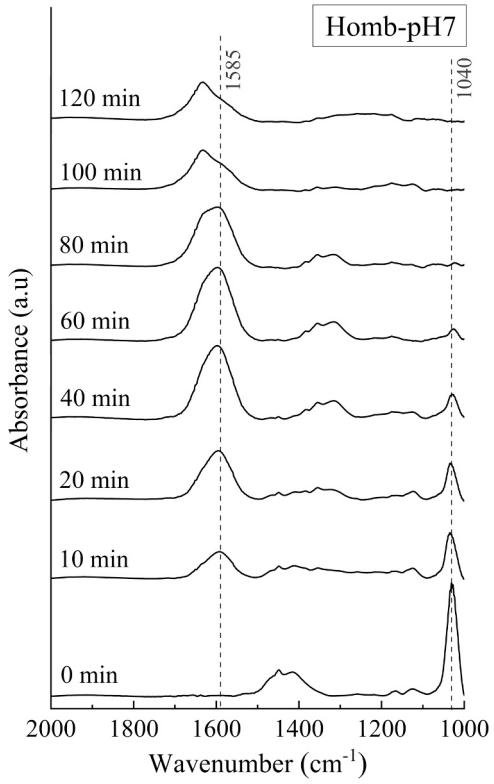

Fig. 7. FT-IR spectra along the time of the photocatalytic degradation of MeOH in Homb-pH7.

$$HCOO^{\bullet} + HO^{\bullet} \rightarrow H_2O + CO_2,\ \Delta G = -142.3\ kcal/mol \quad (24)$$

For the series of reaction towards the degradation of *1*-BuOH and until the formation of carboxylic acids, the $HO^{\bullet}$ radicals participate as oxidising species. Reaction free energies (ΔG), obtained from the DFT calculations, for the photocatalytic oxidation of alcohols, aldehydes, and carboxylic acids (Eqs. 9, 11, and 13) are very similar, so we hypothesise that the non-observation of aldehydes can be attributed to an exergonic tendency in these degradation steps. If carboxylic acids react with the surface forming carboxylates, as it has been observed experimentally, these can only be degraded by h^+ (Eq. 14). In this sense, these direct reactions of the carboxylates with the surface are those indicated as responsible for the deactivation of the catalysts in different photocatalytic processes [63,64]. In fact, in our studies carried out with Hombikat-b and Homb-pH7, a very slow degradation of these compounds has been observed. On the other hand, with the Homb@EST-pH7 composite, the carboxylates adsorbed on the surface are much lower and they degrade relatively quickly when all the *1*-BuOH has been eliminated. The low concentration of carboxylates observed in Homb@EST-pH7 can be attributed to higher rate of $HO^{\bullet}$ radicals' formation, which allows the degradation of carboxylic acids before they are adsorbed on the surface (Eq. 13).

In the studies for the degradation of MeOH with Hombikat-b and Homb-pH7, we observe the degradation of the generated ionic formates once the alcohol has been eliminated. In this regard, since formates are strongly hydrated, they are only observed in ionic form, inhibiting adsorption. Unlike the carboxylates generated from the degradation of *1*-BuOH. Notwithstanding, the degradation of the generated formates with the Homb@EST-pH7 composite is significantly more efficient also for the case of MeOH.

The characterisation studies carried out have shown that the synthesised composite Homb@EST-pH7 is constituted by TiO_2 aggregates of anatase and rutile with size greater than 60 nm, with low surface hydroxylation, presence of electron traps, and low surface from the EST-1023 component. In addition, such aggregates are also covered with highly hydroxylated TiO_2 aggregates with high surface area and size of 2–3 and 8 nm of anatase phase from Hombikat-b.

Hombikat-b and Homb-pH7 are constituted by nanoparticles of 2–3 and 8 nm, which form two types of agglomerates, some with values *ca.* 1.5 μm and others of 62.7 μm. The decrease in particle size increases the surface area of these materials and therefore the number of active centres. However, it has been indicated that in nanoparticles smaller than 10 nm, as in this case, the recombination speed of the e^-/h^+ pair on the surface of the catalyst is significantly increased [65]. Thus, when the concentration of these nanoparticles increases, forming a compact aggregate as observed in Hombikat-b, the photogenerated holes can recombine with the photogenerated electrons from adjacent particles [66]. On the other hand, FT-IR characterisation studies have shown high surface hydration of Hombikat-b and Homb-pH7, which negatively influences the access of O_2 to the photogenerated electrons due to the obstruction caused by the hydrogen bonds of the water molecules with the surface.

Besides, FT-IR studies have also shown the presence of defects, such as oxygen vacancies, in the EST-1023. These defects, together with the slight delocalisation of the molecular orbitals on the surface, lead to the generation of stable shallow electron traps near the edge of the conduction band [67]. Shallow electron traps are not associated with localised structures but are delocalised across the TiO_2 surface. In this

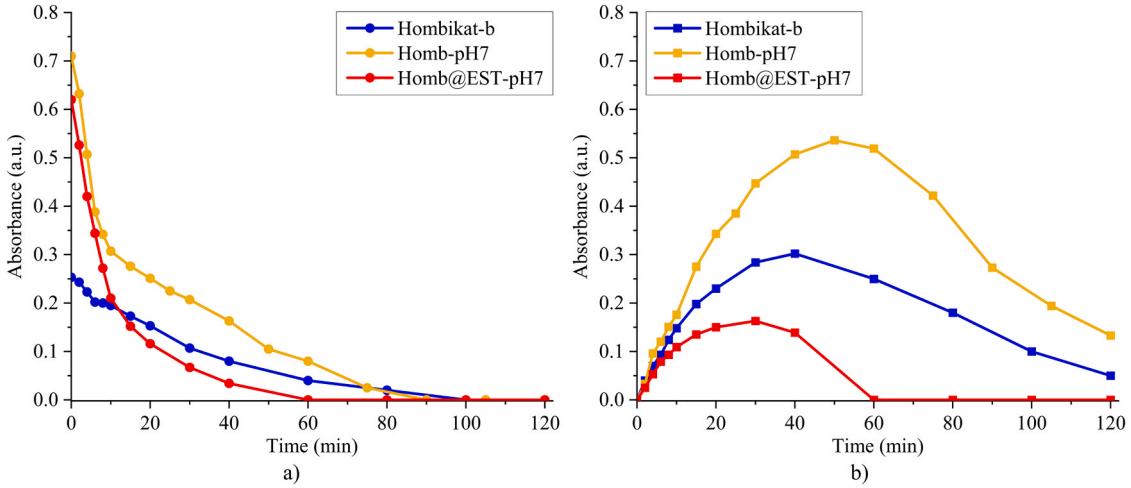

Fig. 8. Evolution of a) adsorbed MeOH (●) and b) generated formates (■) for Hombikat-b, Homb-pH7 and Homb@EST-pH7.

way, the electrons in these centres are not easily recombined with the holes as there are traps that stabilise them, thus reducing the recombination rate and facilitating their reaction with oxygen [68]. Thus, it has been indicated that oxygen vacancies distort the main structural unit of TiO_2, *i.e.*, the TiO_6 octahedron, giving rise to a non-symmetric distribution of the charges generated by electrons in excess around the oxygen vacancy, which generates a dipole moment [69,70]. This dipole moment can influence charge separation, as well as the interaction with other particles, producing the new aggregates observed in Homb@EST-pH7. It has been indicated that the presence of centres with high concentration of OH groups combined with a high crystallinity, which facilitates charge separation [24], gives rise to high catalyst activity [25]. In this case, the presence of centres with high concentration of OH groups (present in the Hombikat nanoparticles) combined with electron-trapping centres (present in the EST-1023 particles) are leading to highly photoactive centres.

The Homb@EST-pH7 composite formed by aggregates of 60–90 nm particles of EST-1023 coated with aggregates of smaller particle sizes of 2–3 and 8 nm of Hombikat-b presents a promised combination for efficient photocatalytic activity in gas phase. The Hombikat-b nanoparticles give the catalyst a high hydrated surface area to interact with the alcohols studied. In additions, the electron traps present in EST-1023 facilitate the separation of charges of the e^-/h^+ pair, increasing the capabilities for the formation of $HO^\bullet$ radicals. Similarly, it has been indicated that in P25 there is a morphology of rutile nanoclusters surrounded by anatase. The transition point between both phases allows the rapid transfer of electrons between phases, converting rutile to an electron sink [8]. In the particular case of Homb@EST-pH7 composite, the photogenerated electrons in the anatase particles of Hombikat-b can be transferred to the electron traps present in the anatase or rutile phases of EST-1023, favouring the greater formation of $HO^\bullet$ radicals in the anatase particles of Hombikat-b. (See Scheme 2).

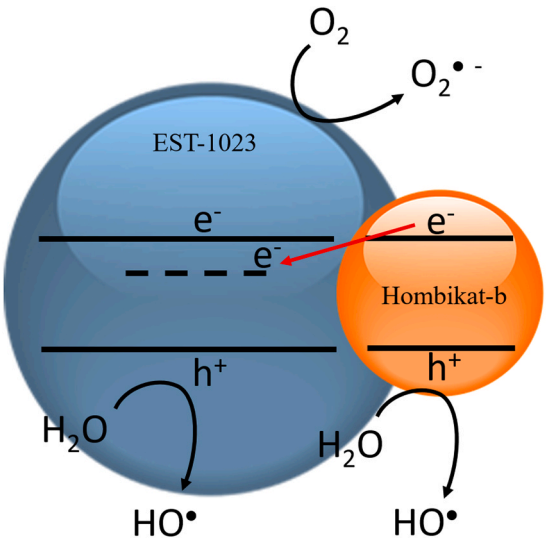

Scheme 2. Schematic representation of the photocatalytic interplay in the heterojuntion of Hombikat-b and EST-1023.

4. Conclusions

For the probe molecules studied, *1*-BuOH and MeOH, the adsorption capabilities are more than ten times higher in the commercial catalyst Hombikat-b and Homb-pH7 than in the EST-1023 and EST-pH7 synthesised in lab. On the other hand, in Hombikat-b and Homb-pH7, the degradation of the alcohols and intermediates formed is very slow. The new synthesised composite Homb@EST-pH7 has an adsorption capacity for the studied alcohols similar to that of Hombikat-b and Homb-pH7, but it has a much higher degradation capacity for *1*-BuOH, MeOH, and the produced intermediates.

It has been determined that in aqueous solution at neutral pH, the aggregates present in EST-pH7 and Homb-pH7 partially disintegrate, and when both catalysts are in contact, an interaction occurs between them. In this way, it has been determined that the Homb@EST-pH7 composite is formed from EST-1023 aggregates covered with Hombikat-b aggregates. The high capacity to produce $HO^\bullet$ radicals of this composite is attributed to the transfer of photogenerated electrons in Hombikat-b to the electron traps present in EST-1023. For its part, the high adsorption capacity is attributed to the high surface area and high hydroxylation conferred by the Homb-pH7 aggregates. In addition, the high capacity to produce $HO^\bullet$ radicals of the Homb@EST-pH7 composite prevents the adsorption of carboxylic acids on the surface of the catalyst, thus avoiding deactivation processes. Attending to these results, we believe that the new composite may be a promising material for photocatalytic applications in the gas phase.

CRediT authorship contribution statement

Óscar M. González-Díaz: Investigation, Project administration, Writing – review & editing. **José Miguel Doña-Rodríguez:** Conceptualization, Methodology, Writing – review & editing. **Alison Robles:** Investigation. **Andrea Illana:** Investigation, Validation, Writing – original draft, Writing – review & editing. **Javier Araña:** Conceptualization, Supervision, Writing – original draft, Writing – review & editing. **Elisenda Pulido-Melián:** Investigation, Project administration, Writing – review & editing. **Luis Miguel Azofra:** Formal analysis, Writing – review & editing.

Declaration of Competing Interest

The authors declare that they have no known competing financial interests or personal relationships that could have appeared to influence the work reported in this paper.

Data availability

Data will be made available on request.

Acknowledgments

We thank the financial support of MCIN (projects refs. PID2020–118720RB-I00 / AEI / 10.13039/501100011033 and EQC2019–006048-P), MINECO (project ref. UNLP10–3E-726), and Cabildo Insular de Gran Canaria (project ref. CABINFR2019–08). A.I. is a Margarita Salas UCM fellow (ref. CT31/21) and thanks the Spanish Ministry of Universities and NextGenerationEU funds for support. L.M. A. is a Ramón y Cajal fellow (ref. RYC2021–030994-I) and thanks MCIN/AEI and NextGenerationEU/PRTR for support. Gratitude is also due to the Instituto de Astrofísica de Canarias (IAC) for providing the computational resources (La Palma Supercomputer), and to National Centre for Electron Microscopy (ICTS-CNME, UCM) for HR-TEM facilities. This Special Issue is dedicated to honour the retirement of Prof Santiago Esplugas at the Universitat de Barcelona (UB, Spain), a key figure in the area of catalytic advanced oxidation processes.

Appendix A. Supporting information

Supplementary data associated with this article can be found in the online version at doi:10.1016/j.cattod.2024.114603.

References

[1] M. Melchionna, P. Fornasiero, Updates on the Roadmap for Photocatalysis, ACS Catal. 10 (2020) 5493–5501, https://doi.org/10.1021/acscatal.0c01204.

[2] L. Candish, K.D. Collins, G.C. Cook, J.J. Douglas, A. Gómez-Suárez, A. Jolit, S. Keess, Photocatalysis in the life science industry, Chem. Rev. 122 (2022) 2907–2980, https://doi.org/10.1021/acs.chemrev.1c00416.

[3] A. Amorós-Pérez, L. Cano-Casanova, A. Castillo-Deltell, M.Á. Lillo-Ródenas, M. del C. Román-Martínez, TiO2 modification with transition metallic species (Cr, Co, Ni, and Cu) for photocatalytic abatement of acetic acid in liquid phase and propene in gas phase, Mater. (Basel) 12 (2019), https://doi.org/10.3390/ma12010040.

[4] H. Wang, X. Li, X. Zhao, C. Li, X. Song, P. Zhang, P. Huo, X. Li, A review on heterogeneous photocatalysis for environmental remediation: from semiconductors to modification strategies, Chin. J. Catal. 43 (2022) 178–214, https://doi.org/10.1016/S1872-2067(21)63910-4.

[5] G. Balasubramanian, D.D. Dionysiou, M.T. Suidan, I. Baudin, J.-M. Laíné, Evaluating the activities of immobilized TiO2 powder films for the photocatalytic degradation of organic contaminants in water, Appl. Catal. B Environ. 47 (2004) 73–84, https://doi.org/10.1016/j.apcatb.2003.04.002.

[6] Y. Chen, D.D. Dionysiou, TiO2 photocatalytic films on stainless steel: the role of Degussa P-25 in modified sol–gel methods, Appl. Catal. B Environ. 62 (2006) 255–264, https://doi.org/10.1016/j.apcatb.2005.07.017.

[7] W. Sangchay, L. Sikong, K. Kooptarnond, Comparison of photocatalytic reaction of commercial P25 and synthetic TiO2-AgCl nanoparticles, Procedia Eng. 32 (2012) 590–596, https://doi.org/10.1016/j.proeng.2012.01.1313.

[8] D.C. Hurum, A.G. Agrios, K.A. Gray, T. Rajh, M.C. Thurnauer, Explaining the enhanced photocatalytic activity of degussa P25 mixed-phase TiO2 using EPR, J. Phys. Chem. B. 107 (2003) 4545–4549, https://doi.org/10.1021/jp0273934.

[9] A.P. Naik, H. Mittal, V.S. Wadi, L. Sane, A. Raj, S.M. Alhassan, A. Al Alili, S. V. Bhosale, P.P. Morajkar, Super porous TiO2 photocatalyst: tailoring the agglomerate porosity into robust structural mesoporosity with enhanced surface area for efficient remediation of azo dye polluted waste water, J. Environ. Manag. 258 (2020) 110029, https://doi.org/10.1016/j.jenvman.2019.110029.

[10] M.J. Uddin, F. Cesano, A.R. Chowdhury, T. Trad, S. Cravanzola, G. Martra, L. Mino, A. Zecchina, D. Scarano, Surface structure and phase composition of TiO2 P25 particles after thermal treatments and HF etching, Front. Mater. 7 (2020), https://doi.org/10.3389/fmats.2020.00192.

[11] L. Liu, X. Gu, C. Sun, H. Li, Y. Deng, F. Gao, L. Dong, In situ loading of ultra-small Cu2O particles on TiO2 nanosheets to enhance the visible-light photoactivity, Nanoscale 4 (2012) 6351–6359, https://doi.org/10.1039/C2NR31859H.

[12] J. He, Y. Du, Y. Bai, J. An, X. Cai, Y. Chen, P. Wang, X. Yang, Q. Feng, Facile formation of anatase/rutile TiO2 nanocomposites with enhanced photocatalytic activity, Molecules 24 (2019), https://doi.org/10.3390/molecules24162996.

[13] B. Basumatary, R. Basumatary, A. Ramchiary, D. Konwar, Evaluation of Ag@TiO2/WO3 heterojunction photocatalyst for enhanced photocatalytic activity towards methylene blue degradation, Chemosphere 286 (2022) 131848, https://doi.org/10.1016/j.chemosphere.2021.131848.

[14] M. Dahl, Y. Liu, Y. Yin, Composite titanium dioxide nanomaterials, Chem. Rev. 114 (2014) 9853–9889, https://doi.org/10.1021/cr400634p.

[15] J. Araña, J.M. Doña-Rodríguez, C.G. i Cabo, O. González-Díaz, J.A. Herrera-Melián, J. Pérez-Peña, FTIR study of gas-phase alcohols photocatalytic degradation with TiO2 and AC-TiO2, Appl. Catal. B Environ. 53 (2004) 221–232, https://doi.org/10.1016/j.apcatb.2004.04.024.

[16] J. Araña, A. Peña Alonso, J.M. Doña Rodríguez, J.A. Herrera Melián, O. González Díaz, J. Pérez Peña, Comparative study of MTBE photocatalytic degradation with TiO2 and Cu-TiO2, Appl. Catal. B Environ. 78 (2008) 355–363, https://doi.org/10.1016/j.apcatb.2007.09.023.

[17] J.C. Yu, J. Yu, W. Ho, L. Zhang, Preparation of highly photocatalytic active nano-sized TiO2 particles via ultrasonic irradiation, Chem. Commun. (2001) 1942–1943, https://doi.org/10.1039/B105471F.

[18] G. Oskam, A. Nellore, R.L. Penn, P.C. Searson, The growth kinetics of TiO2 nanoparticles from titanium(IV) alkoxide at high water/titanium ratio, J. Phys. Chem. B. 107 (2003) 1734–1738, https://doi.org/10.1021/jp021237f.

[19] N. Liu, X. Chen, J. Zhang, J.W. Schwank, A review on TiO2-based nanotubes synthesized via hydrothermal method: formation mechanism, structure modification, and photocatalytic applications, Catal. Today 225 (2014) 34–51, https://doi.org/10.1016/j.cattod.2013.10.090.

[20] G. Arthi, J. Archana, M. Navaneethan, S. Ponnusamy, Y. Hayakawa, C. Muthamizhchelvan, Hydrothermal growth of ligand-passivated high-surface-area TiO2 nanoparticles and dye-sensitized solar cell characteristics, Scr. Mater. 68 (2013) 396–399, https://doi.org/10.1016/j.scriptamat.2012.10.049.

[21] M. Sachs, E. Pastor, A. Kafizas, J.R. Durrant, Evaluation of surface state mediated charge recombination in anatase and rutile TiO2, J. Phys. Chem. Lett. 7 (2016) 3742–3746, https://doi.org/10.1021/acs.jpclett.6b01501.

[22] H. Hou, H. Miyafuji, H. Kawamoto, S. Saka, Supercritically treated TiO2-activated carbon composites for cleaning ammonia, J. Wood Sci. 52 (2006) 533–538, https://doi.org/10.1007/s10086-006-0811-6.

[23] Š. Paušová, L. Pacileo, M. Baudys, A. Hrubantová, M. Neumann-Spallart, D. Dvoranová, V. Brezová, J. Krýsa, Active carbon/TiO2 composites for photocatalytic decomposition of benzoic acid in water and toluene in air, Catal. Today 388–389 (2022) 417–423, https://doi.org/10.1016/j.cattod.2020.06.048.

[24] C. Colbeau-Justin, M. Kunst, D. Huguenin, Structural influence on charge-carrier lifetimes in TiO2 powders studied by microwave absorption, J. Mater. Sci. 38 (2003) 2429–2437, https://doi.org/10.1023/A:1023905102094.

[25] J.T. Carneiro, T.J. Savenije, J.A. Moulijn, G. Mul, Toward a physically sound structure−activity relationship of TiO2-based photocatalysts, J. Phys. Chem. C. 114 (2010) 327–332, https://doi.org/10.1021/jp906395w.

[26] A. Heller, Conversion of sunlight into electrical power and photoassisted electrolysis of water in photoelectrochemical cells, Acc. Chem. Res. 14 (1981) 154–162, https://doi.org/10.1021/ar00065a004.

[27] R. Katoh, A. Furube, K. Yamanaka, T. Morikawa, Charge separation and trapping in N-doped TiO2 photocatalysts: a time-resolved microwave conductivity study, J. Phys. Chem. Lett. 1 (2010) 3261–3265, https://doi.org/10.1021/jz1011548.

[28] J.T. Carneiro, C.-C. Yang, J.A. Moma, J.A. Moulijn, G. Mul, How gold deposition affects anatase performance in the photo-catalytic oxidation of cyclohexane, Catal. Lett. 129 (2009) 12–19, https://doi.org/10.1007/s10562-008-9801-1.

[29] A. Holm, M. Hamandi, F. Simonet, B. Jouguet, F. Dappozze, C. Guillard, Impact of rutile and anatase phase on the photocatalytic decomposition of lactic acid, Appl. Catal. B Environ. 253 (2019) 96–104, https://doi.org/10.1016/j.apcatb.2019.04.042.

[30] D.S. Bhatkhande, V.G. Pangarkar, A.A.C.M. Beenackers, Photocatalytic degradation for environmental applications – a review, J. Chem. Technol. Biotechnol. 77 (2002) 102–116, https://doi.org/10.1002/jctb.532.

[31] D. TE, F. FH, Photocatalytic degradation of carbamazepine, clofibric acid and iomeprol with P25 and Hombikat UV100 in the presence of natural organic matter (NOM) and other organic water constituents. PG - 403-11, (n.d.).

[32] S. Belekbir, M. El Azzouzi, A. El Hamidi, L. Rodríguez-Lorenzo, J.A. Santaballa, M. Canle, Improved photocatalyzed degradation of phenol, as a model pollutant, over metal-impregnated nanosized TiO2, Nanomaterials 10 (2020), https://doi.org/10.3390/nano10050996.

[33] D.E. Santiago, J.M. Doña-Rodríguez, J. Araña, C. Fernández-Rodríguez, O. González-Díaz, J. Pérez-Peña, A.M.T. Silva, Optimization of the degradation of imazalil by photocatalysis: comparison between commercial and lab-made photocatalysts, Appl. Catal. B Environ. 138–139 (2013) 391–400, https://doi.org/10.1016/j.apcatb.2013.03.024.

[34] D.E. Santiago, J. Araña, O. González-Díaz, M.E. Alemán-Dominguez, A.C. Acosta-Dacal, C. Fernandez-Rodríguez, J. Pérez-Peña, J.M. Doña-Rodríguez, Effect of inorganic ions on the photocatalytic treatment of agro-industrial wastewaters containing imazalil, Appl. Catal. B Environ. 156–157 (2014) 284–292, https://doi.org/10.1016/j.apcatb.2014.03.022.

[35] P. Kubelka, F. Munk, An article on optics of paint layers, Z. Tech. Phys. 12 (1931) 593–601.

[36] B.M. Weckhuysen, R.A. Schoonheydt, Recent progress in diffuse reflectance spectroscopy of supported metal oxide catalysts, Catal. Today 49 (1999) 441–451, https://doi.org/10.1016/S0920-5861(98)00458-1.

[37] G. Vincent, P.M. Marquaire, O. Zahraa, Photocatalytic degradation of gaseous 1-propanol using an annular reactor: Kinetic modelling and pathways, J. Hazard. Mater. 161 (2009) 1173–1181, https://doi.org/10.1016/j.jhazmat.2008.04.069.

[38] A.D. Becke, Density-functional exchange-energy approximation with correct asymptotic behavior, Phys. Rev. A. 38 (1988) 3098–3100, https://doi.org/10.1103/PhysRevA.38.3098.

[39] C. Lee, W. Yang, R.G. Parr, Development of the Colle-Salvetti correlation-energy formula into a functional of the electron density, Phys. Rev. B. 37 (1988) 785–789, https://doi.org/10.1103/PhysRevB.37.785.

[40] F. Weigend, R. Ahlrichs, Balanced basis sets of split valence, triple zeta valence and quadruple zeta valence quality for H to Rn: Design and assessment of accuracy, Phys. Chem. Chem. Phys. 7 (2005) 3297–3305, https://doi.org/10.1039/B508541A.

[41] M. Valiev, E.J. Bylaska, N. Govind, K. Kowalski, T.P. Straatsma, H.J.J. Van Dam, D. Wang, J. Nieplocha, E. Apra, T.L. Windus, W.A. de Jong, NWChem: A comprehensive and scalable open-source solution for large scale molecular simulations, Comput. Phys. Commun. 181 (2010) 1477–1489, https://doi.org/10.1016/j.cpc.2010.04.018.

[42] E. Aprà, E.J. Bylaska, W.A. de Jong, N. Govind, K. Kowalski, T.P. Straatsma, M. Valiev, H.J.J. van Dam, Y. Alexeev, J. Anchell, V. Anisimov, F.W. Aquino, R. Atta-Fynn, J. Autschbach, N.P. Bauman, J.C. Becca, D.E. Bernholdt, K. Bhaskaran-Nair, S. Bogatko, P. Borowski, J. Boschen, J. Brabec, A. Bruner, E. Cauët, Y. Chen, G.N. Chuev, C.J. Cramer, J. Daily, M.J.O. Deegan, T.H. Dunning, M. Dupuis, K.G. Dyall, G.I. Fann, S.A. Fischer, A. Fonari, H. Früchtl, L. Gagliardi, J. Garza, N. Gawande, S. Ghosh, K. Glaesemann, A.W. Götz, J. Hammond, V. Helms, E.D. Hermes, K. Hirao, S. Hirata, M. Jacquelin, L. Jensen, B.G. Johnson, H. Jónsson, R.A. Kendall, M. Klemm, R. Kobayashi, V. Konkov, S. Krishnamoorthy, M. Krishnan, Z. Lin, R.D. Lins, R.J. Littlefield, A.J. Logsdail, K. Lopata, W. Ma, A. V. Marenich, J. del Campo, D. Mejia-Rodriguez, J.E. Moore, J.M. Mullin, T. Nakajima, D.R. Nascimento, J.A. Nichols, P.J. Nichols, J. Nieplocha, A. Otero-de-la-Roza, B. Palmer, A. Panyala, T. Pirojsirikul, B. Peng, R. Peverati, J. Pittner, L. Pollack, R.M. Richard, P. Sadayappan, G.C. Schatz, W.A. Shelton, D. W. Silverstein, D.M.A. Smith, T.A. Soares, D. Song, M. Swart, H.L. Taylor, G. S. Thomas, V. Tipparaju, D.G. Truhlar, K. Tsemekhman, T. Van Voorhis, Á. Vázquez-Mayagoitia, P. Verma, O. Villa, A. Vishnu, K.D. Vogiatzis, D. Wang, J. H. Weare, M.J. Williamson, T.L. Windus, K. Woliński, A.T. Wong, Q. Wu, C. Yang, Q. Yu, M. Zacharias, Z. Zhang, Y. Zhao, R.J. Harrison, NWChem: past, present, and future, J. Chem. Phys. 152 (2020) 184102, https://doi.org/10.1063/5.0004997.

[43] S. Mehraz, W. Luo, J. Swiatowska, B. Bezzazi, A. Taleb, Hydrothermal synthesis of TiO2 aggregates and their application as negative electrodes for lithium-ion batteries: the conflicting effects of specific surface and pore size, Mater. (Basel) 14 (2021), https://doi.org/10.3390/ma14040916.

[44] E.M. Hotze, T. Phenrat, G.V. Lowry, Nanoparticle aggregation: challenges to understanding transport and reactivity in the environment, J. Environ. Qual. 39 (2010) 1909–1924, https://doi.org/10.2134/jeq2009.0462.

[45] A. Alonso-Tellez, R. Masson, D. Robert, N. Keller, V. Keller, Comparison of Hombikat UV100 and P25 TiO2 performance in gas-phase photocatalytic oxidation reactions, J. Photochem. Photobiol. A Chem. 250 (2012) 58–65, https://doi.org/10.1016/j.jphotochem.2012.10.008.

[46] M. Wang, B. Nie, K.-K. Yee, H. Bian, C. Lee, H.K. Lee, B. Zheng, J. Lu, L. Luo, Y. Y. Li, Low-temperature fabrication of brown TiO2 with enhanced photocatalytic

activities under visible light, Chem. Commun. 52 (2016) 2988–2991, https://doi.org/10.1039/C5CC09176D.
[47] S.G. Ullattil, R.M. Ramakrishnan, Defect-rich brown TiO2–x porous flower aggregates: selective photocatalytic reversibility for organic dye degradation, ACS Appl. Nano Mater. 1 (2018) 4045–4052, https://doi.org/10.1021/acsanm.8b00824.
[48] D.J.C. Yates, Infrared studies of the surface hydroxyl groups on titanium dioxide, and of the chemisorption of carbon monoxide and carbon dioxide, J. Phys. Chem. 65 (1961) 746–753, https://doi.org/10.1021/j100823a011.
[49] M. Primet, P. Pichat, M.V. Mathieu, Infrared study of the surface of titanium dioxides. I. Hydroxyl groups, J. Phys. Chem. 75 (1971) 1216–1220, https://doi.org/10.1021/j100679a007.
[50] K. Tanaka, J.M. White, Characterization of species adsorbed on oxidized and reduced anatase, J. Phys. Chem. 86 (1982) 4708–4714, https://doi.org/10.1021/j100221a014.
[51] L.A. Phillips, G.B. Raupp, Infrared spectroscopic investigation of gas—solid heterogeneous photocatalytic oxidation of trichloroethylene, J. Mol. Catal. 77 (1992) 297–311, https://doi.org/10.1016/0304-5102(92)80209-Y.
[52] S.H. Szczepankiewicz, A.J. Colussi, M.R. Hoffmann, Infrared spectra of photoinduced species on hydroxylated titania surfaces, J. Phys. Chem. B. 104 (2000) 9842–9850, https://doi.org/10.1021/jp0007890.
[53] D. Panayotov, J.T. Yates, Electron exchange on TiO2–SiO2 photocatalysts during O2 and organic molecule adsorption – the role of adsorbate electrophilicity, Chem. Phys. Lett. 381 (2003) 154–162, https://doi.org/10.1016/j.cplett.2003.09.004.
[54] D.A. Panayotov, J.T. Yates, n-Type doping of TiO2 with atomic hydrogen-observation of the production of conduction band electrons by infrared spectroscopy, Chem. Phys. Lett. 436 (2007) 204–208, https://doi.org/10.1016/j.cplett.2007.01.039.
[55] T.L. Thompson, J.T. Yates, Surface science studies of the photoactivation of TiO2 new photochemical processes, Chem. Rev. 106 (2006) 4428–4453, https://doi.org/10.1021/cr050172k.
[56] A. Yee, S.J. Morrison, H. Idriss, A study of the reactions of ethanol on CeO2 and Pd/CeO2 by steady state reactions, temperature programmed desorption, and in situ FT-IR, J. Catal. 186 (1999) 279–295, https://doi.org/10.1006/jcat.1999.2563.
[57] A.M. Nadeem, G.I.N. Waterhouse, H. Idriss, The reactions of ethanol on TiO2 and Au/TiO2 anatase catalysts, Catal. Today 182 (2012) 16–24, https://doi.org/10.1016/j.cattod.2011.08.051.
[58] W. Rachmady, M.A. Vannice, Acetic acid reduction by H2 over supported Pt catalysts: a DRIFTS and TPD/TPR study, J. Catal. 207 (2002) 317–330, https://doi.org/10.1006/jcat.2002.3556.
[59] Formation of Surface Complexes of Organic Molecules, in: Mol. Spectrosc. Oxide Catal. Surfaces, John Wiley & Sons, Ltd, 2003, pp. 309–458, https://doi.org/10.1002/0470867981.ch5.
[60] J. Raskó, J. Bontovics, F. Solymosi, FTIR study of the interaction of methanol with clean and potassium-doped PdSiO2 catalysts, J. Catal. 146 (1994) 22–33, https://doi.org/10.1016/0021-9517(94)90004-3.
[61] F.P. Rotzinger, J.M. Kesselman-Truttmann, S.J. Hug, V. Shklover, M. Grätzel, Structure and vibrational spectrum of formate and acetate adsorbed from aqueous solution onto the TiO2 rutile (110) surface, J. Phys. Chem. B. 108 (2004) 5004–5017, https://doi.org/10.1021/jp0360974.
[62] A. Hatipoğlu, Z. Çinar, A QSAR study on the kinetics of the reactions of aliphatic alcohols with the photogenerated hydroxyl radicals, J. Mol. Struct. Theochem. 631 (2003) 189–207, https://doi.org/10.1016/S0166-1280(03)00248-3.
[63] A.R. Almeida, J.A. Moulijn, G. Mul, In situ ATR-FTIR study on the selective photo-oxidation of cyclohexane over anatase TiO2, J. Phys. Chem. C. 112 (2008) 1552–1561, https://doi.org/10.1021/jp077143t.
[64] F. Thevenet, C. Guillard, A. Rousseau, Acetylene photocatalytic oxidation using continuous flow reactor: gas phase and adsorbed phase investigation, assessment of the photocatalyst deactivation, Chem. Eng. J. 244 (2014) 50–58, https://doi.org/10.1016/j.cej.2014.01.038.
[65] Z. Zhang, C.-C. Wang, R. Zakaria, J.Y. Ying, Role of particle size in nanocrystalline TiO2-based photocatalysts, J. Phys. Chem. B 102 (1998) 10871–10878, https://doi.org/10.1021/jp982948.
[66] D. Jassby, J. Farner Budarz, M. Wiesner, Impact of aggregate size and structure on the photocatalytic properties of TiO2 and ZnO nanoparticles, Environ. Sci. Technol. 46 (2012) 6934–6941, https://doi.org/10.1021/es202009h.
[67] H. Lin, C.P. Huang, W. Li, C. Ni, S.I. Shah, Y.-H. Tseng, Size dependency of nanocrystalline TiO2 on its optical property and photocatalytic reactivity exemplified by 2-chlorophenol, Appl. Catal. B Environ. 68 (2006) 1–11, https://doi.org/10.1016/j.apcatb.2006.07.018.
[68] D. Li, H. Song, X. Meng, T. Shen, J. Sun, W. Han, X. Wang, Effects of particle size on the structure and photocatalytic performance by alkali-treated TiO2, Nanomaterials 10 (2020), https://doi.org/10.3390/nano10030546.
[69] V. Bessergenev, High-temperature anomalies of dielectric constant in TiO2 thin films, Mater. Res. Bull. 44 (2009) 1722–1728, https://doi.org/10.1016/j.materresbull.2009.03.014.
[70] V.G. Bessergenev, M.C. Mateus, A.M.B. do Rego, M. Hantusch, E. Burkel, An improvement of photocatalytic activity of TiO2 Degussa P25 powder, Appl. Catal. A Gen. 500 (2015) 40–50, https://doi.org/10.1016/j.apcata.2015.05.002.